Available online at www.sciencedirect.com
SCIENCE DIRECT®
Journal of Magnetic Resonance 174 (2005) 292–300
JMR Journal of Magnetic Resonance
www.elsevier.com/locate/jmr

Electromagnetic characterization of rectangular ferroelectric resonators

Ilia Geifman [a,*], Iryna S. Golovina [b]

[a] EMS Inc., 165 King Street, Elk Grove Village, IL 60007, USA
[b] Institute of Semiconductor Physics of NASU, pr.Nauki 45, 03028 Kiev, Ukraine

Received 30 December 2004; revised 14 February 2005
Available online 26 March 2005

Abstract

An optimized geometry for a rectangular ferroelectric resonator (FR) is proposed to increase signal-to-noise ratio in EPR spectroscopy. To develop optimization criteria, the distribution of the microwave electromagnetic field in the FR is computed and analyzed. The computations, based on solution of Maxwell's field equations, were made for two types of rectangular FRs—a FR with a hollow sample hole and a FR with a blind sample hole. To introduce the samples, a hole was drilled through the resonator with its axis aligned to the axis of the FR. We computed and studied the spatial distributions of *H*- and *E*-components of the microwave electromagnetic field for two rectangular FRs, made of single-crystal potassium tantalate, with the following sizes: $1.9 \times 1.9 \times 1.4\ \text{mm}^3$ and $1.7 \times 1.7 \times 3.1\ \text{mm}^3$. As analysis of the obtained data indicated, in both resonators, the lowest mode was $TE_{11\delta}$. By analyzing the distribution of the microwave field in the FR and comparing it with the experimental result, we developed optimization criteria for the geometry of a rectangular FR.

Keywords: Microwave electromagnetic field; A ferroelectric resonator; Electron paramagnetic resonance; Potassium tantalate

1. Introduction

Applications of the EPR method in medicine and research of biological objects demand increased sensitivity in EPR spectrometers [1]. A method of increasing sensitivity is the use of dielectric resonators (DRs) [2–9]. FRs are a subclass of DRs, which have recently attracted the attention of researchers [10–14]. FRs possess a number of advantages and have a potentially higher efficiency in comparison with other DRs due to a high dielectric constant and the opportunity to control it.

Recently, single-crystal FRs of cylindrical [13,14] and rectangular [10–12] forms were developed and tested, working in $TE_{01\delta}$ mode. Furthermore, it is possible to have a $TE_{11\delta}$ oscillation as the lowest type of electromagnetic oscillations in rectangular dielectric resonators. This type of oscillations is the most widely used and is suitable for EPR measurements, since the magnetic field has a maximum along the longitudinal axis of the resonator; thus, a DR can be considered equivalent to a magnetic dipole [15].

The full characteristic of any resonator includes the image of intensity distribution of the electromagnetic field. This information can be used in the optimization of the form and dimensions of the resonator, as well as of the location of the sample. In some cases, it is even possible to have the sample outside of the resonator, thus creating conditions for studies in vivo.

The purpose of the present work is to obtain a detailed picture of the spatial distribution of the microwave (MW) electromagnetic field in the rectangular FRs during excitation (such as oscillations of type

* Corresponding author. Fax: +1 847 718 1149.
E-mail addresses: geifmani@yahoo.com (I. Geifman), golovina@isp.kiev.ua (I.S. Golovina).

1090-7807/$ - see front matter © 2005 Elsevier Inc. All rights reserved.
doi:10.1016/j.jmr.2005.02.017

$TE_{11\delta}$), to carry out an analysis of the calculated dependencies, and to compare the computed and experimental results. The ultimate goal is to optimize the dimensions and geometry of a rectangular FR for the achievement of the highest EPR spectrometer sensitivity.

2. Methods

2.1. Material and experimental details

We designed six rectangular resonators made of single-crystal potassium tantalate ($KTaO_3$). This material has a cubic structure and remains paraelectric up to 4.2 K, and is usually called a virtual ferroelectric. For $KTaO_3$, the dielectric constant, ε, at $T > 30$ K obeys the relation: $\varepsilon = B + C/(T - T_c)$, where $B = 45$, $C = 64{,}000$ K, $T_c = 4$ K [16]. In other articles $B = 48$, $C = 57{,}000$ K, $T_c = 4$ K [17]; $B = 48$, $C = 59{,}900$ K, $T_c = 4$ K [18] or $B = 48$, $C = 50{,}000$ K, $T_c = 13$ K [19]. At temperature $T < 30$ K, $\varepsilon = B + C/(0.5 \times T_1 \times \mathrm{cth}(T_1/2T) - T_o)$, where $B = 48$, $C = 50{,}000$ K, $T_c = 13$ K, $T_1 = 55$ K [19]. In our crystals, $\varepsilon = 261$ at 300 K, $\varepsilon = 840$ at $T = 77$ K, and $\varepsilon = 4000$ at $T = 4.2$ K. Normally, dielectrics have a significantly smaller dielectric constant. Generally, the form of the temperature dependence of dielectric constant of $KTaO_3$ is similar to that of ferroelectrics in their paraelectric phase. In these temperature dependences there is a part that obeys the Curie law. Therefore, we consider a resonator made of $KTaO_3$ as a ferroelectric one. There are some unique properties of potassium tantalate that make it attractive. The dielectric constant of $KTaO_3$ can be changed and controlled by external conditions. For instance, by applying an external electric field, as shown in Fig. 1, the temperature dependence of ε becomes smoother. This flexible behavior of ε is convenient and applicable in the design of resonators, depending on their particular usage.

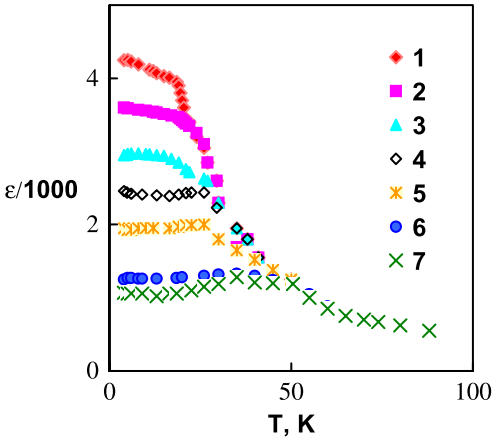

Fig. 1. Dielectric constant, ε, of $KTaO_3$ versus temperature in external electric field, E, kV/cm: 1, 0; 2, 1.25; 3, 3; 4, 4.25; 5, 6; 6, 10; and 7, 15.

Moreover, its exceptionally low dielectric losses $tg\delta = 3.6 \times 10^{-5}$ that correspond to high quality $Q \cong 2.8 \times 10^4$ were recorded at 4.2 K and 13.6 GHz [20]. Dielectric losses decrease as its dielectric susceptibility increases with decreasing temperature [16].

The growth of $KTaO_3$ was carried out in an atmosphere of H_2, O_2, or a vacuum using the Czochralski method [21]. A detailed description can be found elsewhere [12].

The crystals used for the resonators were tested with an X-band CW EPR spectrometer at room and liquid nitrogen temperatures. No background signals were observed.

The EPR experiments were performed with a CW RE-1307 spectrometer, in the temperature range of 77–400 K, at X-band. The FR was placed either inside a short-circuited waveguide section or a standard TE_{011} metal cavity, at the maximum magnetic field. In the case of a waveguide, critical coupling was achieved by a moving short. When using a cavity, the axes of the sample holder and of the FR (in vertical or horizontal position) were parallel to the microwave magnetic field and perpendicular to the DC magnetic field, as is shown in Fig. 2.

Temperatures within the range 77–300 K were attained by blowing nitrogen vapor (liquid nitrogen was heated by an electric heater, which was controlled by a temperature stabilizer) and controlled by a resistor thermometer. A thermometer was fixed to the sample holder at 2 mm above the resonator and the gradient in temperature was taken into account.

To obtain the effect of the FR, G, we recorded S/N in the FR-TE_{011} resonant structure and in the cylindrical TE_{011} cavity alone at same incident power, modulation amplitude, and temperature. The gain (G) is the ratio between the first and the second S/N ratio. In all experiments is used non-saturable sample. The sample used was a single-crystal plate of $ZnS:Mn^{2+}$ with dimensions $0.9 \times 2.0 \times 0.28$ mm^3.

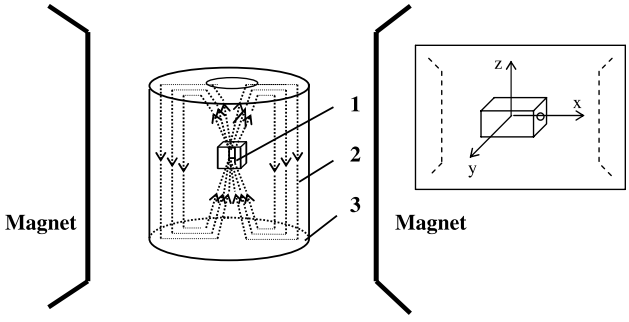

Fig. 2. Location of the FR-TE_{011} resonant structure relative to the DC magnetic field direction: 1, a ferroelectric resonator; 2, microwave magnetic field H_1; and 3, standard TE_{011} cavity. (Inset) Representation of coordinate system and a FR in horizontal position (in this case axis x is parallel to DC magnetic field).

The gain, G, of the FR is caused by increased power conversion factor Cp, which is given by $\mathrm{Cp} = B_1/\sqrt{P}$, where B_1 is a MW magnetic flux density in the resonator, and P is an incident MW power. As incident power was the same in both TE_{011}-FR resonant structure and cylindrical TE_{011} cavity alone, the efficiency of the FR is mostly defined by the MW magnetic field on the sample.

2.2. Theoretical

The expressions for E and H fields are derived within the following assumptions: (1) $H_z = 0$ at all surfaces parallel to the z axis (perfect open-circuit boundary conditions); (2) the tangential E and H fields are continuous across surfaces perpendicular to the z axis, and the fields outside the resonator decay exponentially from its value at the boundary to zero at infinity (Fig. 3); and (3) the resonators are dielectrically isotropic.

Obtained characteristic equations define the resonance frequencies of FR and take into account the dependence of the transverse wave numbers on the resonator parameters.

Below are the final formulas for H- and E-components of $TE_{11\delta}$ mode (in this case $E_z = 0$) used in the computations [15].

Inside the resonator ($|z| \leqslant L/2$):

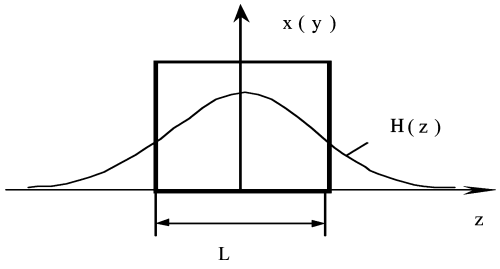

Fig. 3. Model of the MW H-field configuration along axis z of a FR shows how electromagnetic wave penetrates upper and lower boundaries of the resonator under the assumption that MW field changes by sinusoidal low inside and decays exponentially outside resonator.

$$
\begin{aligned}
H_z &= H_0 \cos(\beta_x x)\cos(\beta_y y)\cos(\beta_z z);\\
H_x &= -(\beta_x\beta_z/\beta^2)H_0 \sin(\beta_x x)\cos(\beta_y y)\sin(\beta_z z);\\
H_y &= -(\beta_y\beta_z/\beta^2)H_0 \cos(\beta_x x)\sin(\beta_y y)\sin(\beta_z z);\\
E_x &= j(2\pi\nu\mu_0\beta_y/\beta^2)H_0 \cos(\beta_x x)\sin(\beta_y y)\cos(\beta_z z);\\
E_y &= -j(2\pi\nu\mu_0\beta_x/\beta^2)H_0 \sin(\beta_x x)\cos(\beta_y y)\cos(\beta_z z).
\end{aligned}
\tag{1}
$$

Outside the resonator ($|z| \geqslant L/2$):

$$
\begin{aligned}
H_{0z} &= H_0 \cos(\beta_x x)\cos(\beta_y y)\cos(L\beta_z/2)\exp(\beta_{0z}(L/2-z));\\
H_{0x} &= -(\beta_x\beta_z/\beta^2)H_0 \sin(\beta_x x)\cos(\beta_y y)\sin(L\beta_z/2)\exp(\beta_{0z}(L/2-z));\\
H_{0y} &= -(\beta_y\beta_z/\beta^2)H_0 \cos(\beta_x x)\sin(\beta_y y)\sin(L\beta_z/2)\exp(\beta_{0z}(L/2-z));\\
E_{0x} &= j(2\pi\nu\mu_0\beta_y/\beta^2)H_0 \cos(\beta_x x)\sin(\beta_y y)\cos(L\beta_z/2)\exp(\beta_{0z}(L/2-z));\\
E_{0y} &= -j(2\pi\nu\mu_0\beta_x/\beta^2)H_0 \sin(\beta_x x)\cos(\beta_y y)\cos(L\beta_z/2)\exp(\beta_{0z}(L/2-z)).
\end{aligned}
\tag{2}
$$

Here the x, y, z coordinate system has the origin located at the geometrical center of the resonator (Fig. 2); L is the length of the resonator; and H_0 denotes magnetic field amplitude (we assume $H_0 = 1$). The longitudinal and transverse wave numbers are defined as follows:

$$
\begin{aligned}
&\beta_x = m\pi/A,\ \beta_y = n\pi/B,\ \beta_z = \pi\delta/L,\ \beta_0 = 2\pi\nu(\varepsilon_0\mu_0)^{1/2};\\
&\beta^2 = \beta_x^2 + \beta_y^2;\\
&\beta_z^2 = -(\beta_x^2 + \beta_y^2) + \beta_0^2\varepsilon;\\
&\beta_{0z}^2 = (\beta_x^2 + \beta_y^2) - \beta_0^2;\\
&\beta_{0z} = \beta_z \tan(L\beta_z/2).
\end{aligned}
$$

Here A and B are the width and height of the resonator, respectively; m, n are the integers; δ is a wave attenuation length; and ε is a dielectric constant of the resonator.

The resonant frequency, ν, of the dominant mode for a rectangular ($TE_{11\delta}$) resonator can be defined from the expressions [15]:

$$
\nu = (\beta_x^2 + \beta_y^2 + \beta_z^2)^{1/2}/(2\pi(\varepsilon\varepsilon_0\mu_0)^{1/2}) \tag{3}
$$

taking into account that $\beta_z \tan(L\beta_z/2) = (\beta_x^2 + \beta_y^2 - \beta_0^2)^{1/2}$.

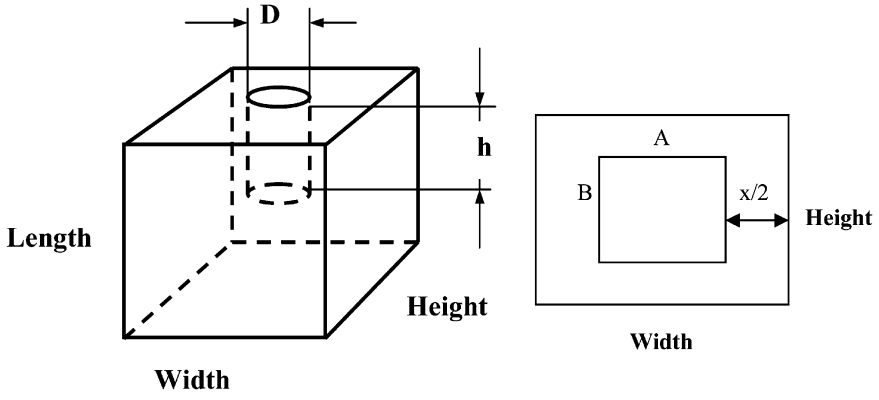

Fig. 4. Schematic pictures of a FR with notations used in Table 1 and Eqs. (1)–(3): (A) real FR with hole for introduction of the sample; (B) model FR (upper view) with dimensions Height and Width reduced to A and B.

Table 1
Characteristics of rectangular ferroelectric resonators used for increasing the sensitivity of the EPR method

Line No.	Resonator	Width (mm)	A (mm)	Height (mm)	B (mm)	Length (mm)	L (mm)	D (mm)	h (mm)	v (MHz)	T (°C)	ε	G	m	n	δ
1.	#1exp	1.9	1.72	1.9	1.72	1.4	1.4	0.9	1.4	9321	300	—	27	—	—	—
2.	#1calc	1.8	1.61	1.8	1.61	1.4	1.4	0.9	1.4	9298	300	261	—	1	1	0.68
3.	#2exp	1.7	1.5	1.7	1.5	3.1	3.1	0.9	3.1	9174	285	—	44	—	—	—
4.	#2calc	1.66	1.45	1.66	1.45	3.1	3.1	0.9	3.1	9182	285	272	—	1	1	0.83
5.	#2exp	1.7	1.5	1.7	1.5	3.1	3.1	0.9	3.1	9174	142	—	29.6	—	—	—
6.	#2calc	1.66	1.45	1.66	1.45	3.1	3.1	0.9	3.1	9352	142	508		2	0	0.872
7.	#3exp	1.8	1.61	1.8	1.61	1.4	1.4	0.9	1.4	9143	165	—	28.5	—	—	—
8.	#3calc	1.8	1.61	1.8	1.61	1.4	1.4	0.9	1.4	9143	148	489	—	2	0	0.744
9.	#3exp	1.8	1.61	1.8	1.61	1.4	1.4	0.9	1.4	9143	267	—	12	—	—	—
10.	#3calc	1.8	1.61	1.8	1.61	1.4	1.4	0.9	1.4	9141	288	270	—	1	1	0.68
11.	#4exp	2.8	2.21	2.6	2.01	3.4	3.4	1.9	2.0	9242	331	—	16	—	—	—
12.	#4calc	2.76	2.16	2.6	2.01	3.4	3.4	1.9	2.0	9269	331	241	—	2	0	0.835
13.	#4exp	2.8	2.8	2.6	2.6	3.4	1.4	0	0	9152	331	—	16	—	—	—
14.	#4calc	2.8	2.8	2.6	2.6	3.4	1.4	0	0	9242	331	241	—	2	1	0.667
15.	#5exp	1.5	1.27	1.5	1.27	3.1	3.1	0.9	1.5	9250	215	—	37	—	—	—
16.	#5calc	1.5	1.27	1.5	1.27	3.1	3.1	0.9	3.1	9250	217	345	—	1	1	0.847
17.	#5exp	1.5	1.27	1.5	1.27	3.1	3.1	0.9	1.5	9129	120	—	35	—	—	—
18.	#5calc	1.5	1.27	1.5	1.27	3.1	3.1	0.9	3.1	9128	105	679	—	2	0	0.885
19.	#5exp	1.5	1.5	1.5	1.5	3.1	1.6	0	0	9279	150	—	31	—	—	—
20.	#5calc	1.5	1.5	1.5	1.5	3.1	1.6	0	0	9279	137	526	—	2	0	0.777
21.	#6exp	2.75	2.26	3.5	3.01	4.6	4.6	1.9	3.0	9124	295	—	10	—	—	—
22.	#6calc	2.73	2.23	3.48	2.98	4.6	4.6	1.9	4.6	9123	295	265	—	2	1	0.877
23.	#6exp	2.75	2.75	3.5	3.5	4.6	1.6	0	0	9124	267	—	4	—	—	—
24.	#6calc	2.75	2.75	3.5	3.5	4.6	1.6	0	0	9124	267	288	—	1	3	0.718

To account for the sample hole in computing the frequency, we subtracted the volume of the hole from the volume of the whole resonator, as follows. The cross-section of a rectangular FR is $S = \text{Width} \cdot \text{Height}$, and the cross-section of the hole is $s = \pi D^2/4$ (see Fig. 4 for notations). By subtracting the area of the cross-section of the hole, we have $\Delta S = S - s$. ΔS is an area of the cross-section of the solid resonator when the hole was subtracted. On the other hand, $\Delta S = A \cdot B$, where $A = \text{Width} - x$, $B = \text{Height} - x$. Hence, $S - s = (\text{Width} - x) \cdot (\text{Height} - x)$. Thus, after calculating x, we have A and B, which are used in Eqs. (1)–(3). For example, for FR #1 (see Table 1), which has Width = 1.9 mm, Height = 1.9 mm, Length = 1.4 mm, and hole of $D = 0.9$ mm, the following values were used in the calculations: $A = 1.72$ mm, $B = 1.72$ mm, and $L = 1.4$ mm. As seen below, such an approach allowed us to obtain resonator parameters reasonable for EPR applications.

3. Results

In Table 1 the calculated and experimental parameters for six rectangular FRs, with hollow sample holes (FRs #1, 2, 3) and with blind sample holes (FRs #4, 5, 6), are presented. Note that in the FR (for example, #2) several $TE_{mn\delta}$ modes ($m = 1$, $n = 1$; $m = 2$, $n = 0$; and $m = 3$, $n = 0$) can be excited due to the temperature dependence of the dielectric constant, ε, of the resonator. Subsequently, as shown in Figs. 5–7, correspondent maximum values of gain, G, in EPR signal intensity are observed. The points when $G = 0$ in the dependence $G(T)$ indicate off-resonant conditions.

Sometimes it is convenient (in particular, for powder or liquid samples) to use in EPR experiments an FR with a blind hole. In our experiments examples of such types of resonators were #4, #5, and #6. For instance, in FR #5, the full length of which is 3.1 mm, there is a hole of depth $h = 1.5$ mm and diameter $D = 0.9$ mm. As shown in Fig. 8, we consider an FR with a blind hole as a complex resonator, consisting of two parts (simple resonators): a lower part I (without hole) has length

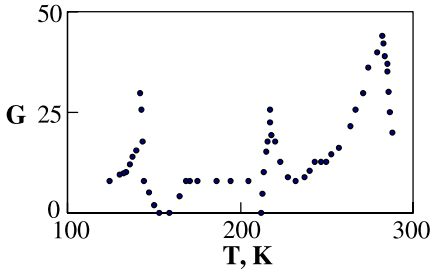

Fig. 5. The effect G of the FR #2 as a function of temperature. Peaks of G correspond to different $TE_{mn\delta}$ modes (see Table 1).

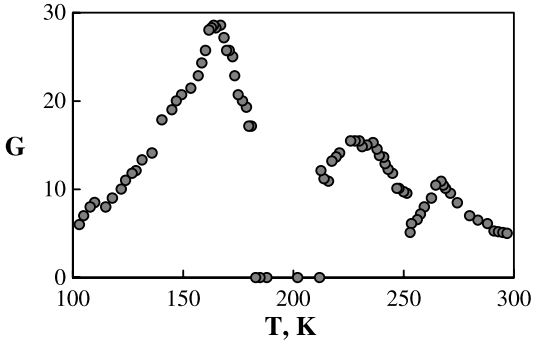

Fig. 6. Gain (G) as a function of temperature for FR #3.

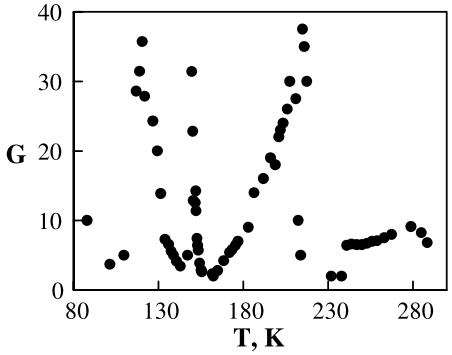

Fig. 7. Gain (G) as a function of temperature for FR #5.

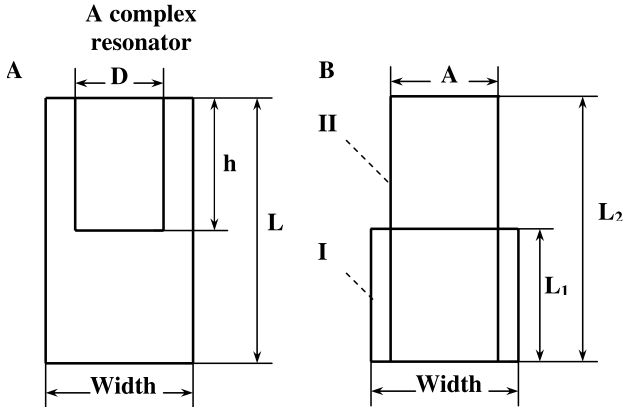

Fig. 8. Structure (A) and substructures (B) of a complex resonator with notations. A FR with a blind hole is considered as a complex resonator (A), consisting of two simple resonators (B): the first simple resonator has dimensions Width $\times L_1$; the second simple resonator has dimensions $A \times L_2$.

$L_1 = L - h$ and an upper part II (with hole) has length $L_2 = L$. For FR #5 the upper part II has length $L = 3.1$ mm, but the width (A) and height (B) must be obtained by taking the hole into account. For this reason, the area of cross-section is reduced by the area of the cross-section of the hole $s = \pi D^2/4$. Therefore, the square root from the result gives $A = B = 1.27$ mm.

3.1. Field computation and comparison with experiment

The results of the field computations are presented for two FRs, #1 and #2, because the general tendency for the other resonators is similar to these two. Also presented are the results of the calculations made for FR #2 while it is in a horizontal position inside a metal cavity and its longest side is parallel to static magnetic field, as is shown in the inset of Fig. 2. All H- and E- components in graphs and tables are presented in relative units.

FR #1: $1.9 \times 1.9 \times 1.4\ \text{mm}^3$, hole diameter $D = 0.9$ mm, $\varepsilon = 261$. Calculated dimensions and parameters: $A = B = 1.61$ mm, $L = h = 1.4$ mm, $\nu = 9298$ MHz, $\delta = 0.6785$, $m = n = 1$.

In Tables 2–4 selected values of H- and E-fields are presented. More detailed dependences of the H_z and E_y components in z and x directions can be seen in Figs. 9 and 10. Fig. 9 shows the decrease of H_z versus distance from the center of the resonator along the z axis, i.e., when a sample is being elevated. Fig. 10A represents the 3D pattern of the changing H_z-field versus distance along z and x axes simultaneously. It was observed that at the lateral wall of the FR (at $x = 0.8$ mm) the H_z-field is very low. The H-field plays an integral role in EPR experiments. However, in order to view a whole picture, the dependence of the E-field is also calculated and presented in Fig. 10B. The E-field can be useful in experiments on paraelectric resonance (PER) and is also important for determining the size of lossy sample, such as aqueous. Note that H- and E-fields in Figs. 9–12 are presented in relative units.

Table 2
H_z-component of MW field versus distance in z direction (at $x = 0$ mm) of FR #1

z (mm)	0	0.1	0.3	0.5	0.7
H_z	1	0.98844	0.89758	0.72422	0.48429
z (mm)	0.8	0.9	1.1	1.2	1.3
H_{0z}	0.36788	0.27945	0.16125	0.12249	0.09305

H_z denotes the magnetic field inside the FR; H_{0z} denotes the magnetic field outside the FR.

Table 3
H_z-component of MW field versus distance in x and z directions of FR #1

$z = 0$ mm							
x (mm)	0	0.1	0.2	0.3	0.4	0.6	0.8
H_z	1	0.98	0.92	0.83	0.71	0.39	0.01
x (mm)	1	1.3	1.61				
H_{0z}	−0.37	−0.82	−1				
$x = 0.8$ mm							
z (mm)	0	0.1	0.3	0.5	0.7		
H_z	0.0105	0.0104	0.0094	0.0076	0.0051		
z (mm)	0.9	1.1	1.3				
H_{0z}	0.0030	0.0017	0.0009				

Table 4
E-component of MW field versus distance in z direction of FR #1

$x = 0$ mm				
z (mm)	0	0.3	0.5	0.7
$E_x = E_y$	0	0	0	0
z (mm)	0.9	1.1	1.3	
$E_{0x} = E_{0y}$	0	0	0	
$x = 0.8$ mm				
E_x	0	0	0	0
E_y	−18.9	−16.9	−13.7	−9.1
E_{0x}	0	0	0	
E_{0y}	−5.3	−3	−1.8	

E_x, E_y denote the electric field inside the FR; E_{0x}, E_{0y} denote the electric field outside the FR.

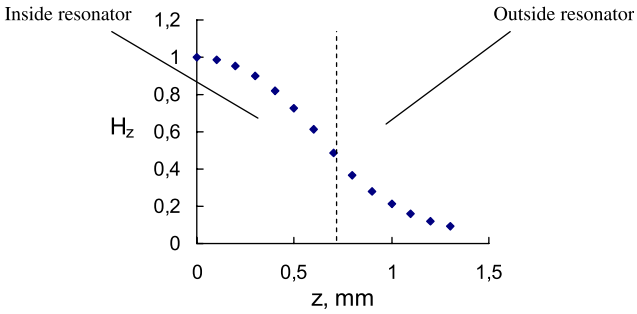

Fig. 9. H_z-field versus distance from the center ($z = 0$) of the resonator along z axis at $x = 0$ (inside and outside the FR #1). See coordinate system representation in Fig. 2.

FR #2: $1.7 \times 1.7 \times 3.1\ \text{mm}^3$, hole diameter $D = 0.9$ mm, $\varepsilon = 272$. Calculated dimensions and parameters: $A = B = 1.45$ mm, $L = h = 3.1$ mm, $\nu = 9182$ MHz; $\delta = 0.8296$, $m = n = 1$.

In Table 5, selected values of H-fields for FR #2 are presented. More detailed dependences of H- and E-fields in z and x directions can be seen in Fig. 11.

FR #2 is in horizontal position. Calculated dimensions and parameters: $A = 3.1$ mm, $B = L = 1.45$ mm, $\nu = 9626.9$ MHz; $\delta = 0.6992$, $m = 2$, $n = 1$.

Fig. 12 illustrates the changes of the H_z-field in (zx) and (zy) planes when FR #2 is in horizontal position. Comparing Fig. 12A with Fig. 12B, it was observed that magnetic field (H_z) contains two half-waves along longer side A, and one half-wave along shorter side B of the FR. Selected computed and experimental values are presented in Table 6.

4. Discussion

We measured the intensities of the EPR signal after changing the location of the sample inside and outside the FR #2. Several experimental values are presented in Table 5. Note that the maximum magnetic field is at the center of the FR. We measured intensity of

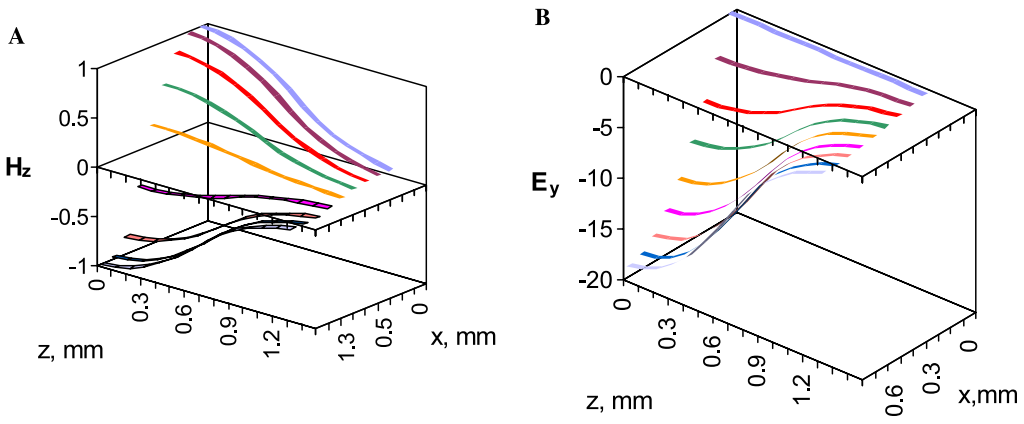

Fig. 10. Distribution of H-fields (A) and E-fields (B) in FR #2. H-field (A) and E-field (B) versus distances along z and x axes for FR #1. Coordinate system is represented in Fig. 2.

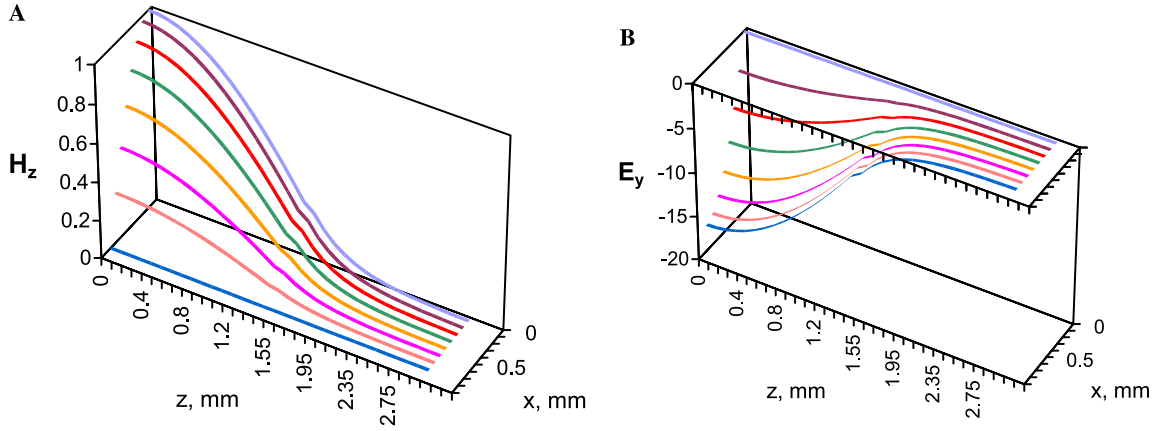

Fig. 11. Distribution of H-fields (A) and E-fields (B) along z and x axes of the FR #2. Coordinate system is represented in Fig. 2.

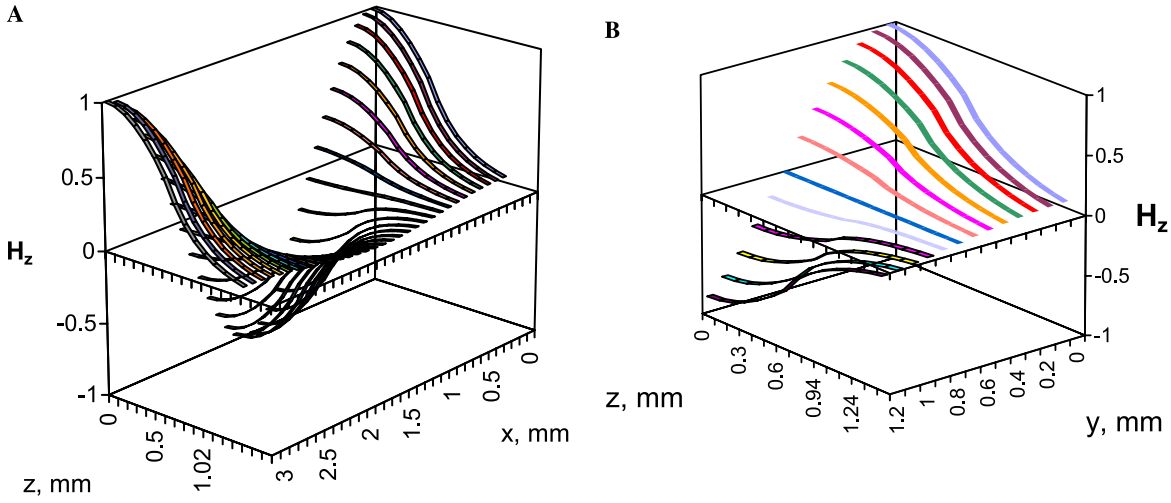

Fig. 12. H-field versus distances in (zx) and (zy) planes for FR #2 in horizontal position. See coordinate system and horizontal position of the resonator in inset of Fig. 2.

EPR line at the center of the FR, and then we measured intensity of EPR line in the location of the sample under the same conditions (MW power, modulation amplitude, temperature). For comparison to calculated value, experimental values are represented as a ratio of signal intensity in the center of the FR (at $x = 0$, $y = 0$,

Table 5
Selected computed and experimental values in z and x directions of FR #2

$x = 0$ mm										
z (mm)	0	0.3	0.7	1.1	1.55					
H_z										
Comp	1	0.97	0.83	0.6	0.265					
Exper	1				0.33					
z (mm)	1.75	2.1	2.55	3.2						
H_{0z}										
Comp	0.14	0.05	0.012	0.0015						
Exper		0.12	0.05	0.033						
$x = 0.725$ mm										
z (mm)	0	0.1	0.3	0.5	0.7	0.8	1	1.2	1.4	1.55
H_z										
Comp	8e−4	8e−4	8e−4	7e−4	7e−4	6e−4	5e−4	4e−4	3e−4	2e−4
$z = 0$ mm										
x (mm)	0	0.2	0.3	0.4	0.5	0.6	0.725	0.734		
H_z										
Comp	1	0.908	0.796	0.648	0.469	0.268	0.0008	−0.03		

Table 6
Selected computed and experimental values in (zx) and (zy) planes for FR #2 in horizontal position

$x = 0$, $y = 0$ mm				
z (mm)	0	0.3	0.5	0.7
H_z				
Computed	1	0.90	0.73	0.49
Experimental	1			
Z (mm)	0.85	0.95	1.25	1.4
H_{0z}				
Computed	0.32	0.24	0.09	0.06
Experimental	0.33			
$z = 0$, $y = 0$ mm				
x (mm)	0	0.5	0.7	1.55
H_z				
Computed	1	0.53	0.15	−1
Experimental	1			8e−3
X (mm)	1.7	1.9	2.1	2.3
H_{0z}				
Computed	−0.95	−0.76	−0.4	−0.05
Experimental				
$z = 0$, $x = 0$ mm				
y (mm)	0	0.3	0.5	0.72
H_z				
Computed	1	0.79	0.46	8e−4
Experimental	1			
Y (mm)	0.85	0.9	1.25	1.4
H_{0z}				
Computed	−0.27	−0.4	−0.9	−1
Experimental	0.04			

$z = 0$) to that in the sample location. It should also be noted that experimental values presented in Table 5 correspond to the location of the mid-point of the sample. Taking into account the length of the sample is 2.0 mm, the experimental value should be compared with both, the computed value at relevant coordinate of z, and computed values in the interval $z - 1 < z < z + 1$ mm. In other words, when the location of the sample changes along z axis, experimental values should be compared with averaged H_z values within the $z - 1 < z < z + 1$ mm interval. According to Table 5, the experimental and computed values are in a qualitative agreement. When a comparison is made in the (xy) plane, it should also be taken into account that the sample is not a point. In this case, the width of the sample performs the main role. For example, at $z = 0$ and $x = 0.72$ mm (on the border of the FR) the experimental value is 0.04. It is larger, than the calculated one, because the width of the sample constitutes 0.28 mm, and the greater part of the sample is located at some distance (up to 0.28 mm) from the border of the FR. As our calculations demonstrate, the computed value of the H_z-field at $z = 0$ and $x = 0.734$ mm is -0.03. Thus, in the (xy) plane the field is larger at the location of the sample than on the border of the FR.

When FR #2 was in a horizontal position in the center of metal cavity (see inset in Fig. 2), we measured the EPR signal on the upper surface (at $x = 0$, $y = 0$, $z = 0.85$ mm), lateral surface (at $z = 0$, $x = 0$ mm, $y = 0.85$ mm), and at the end of the longest dimension (at $z = 0$, $y = 0$ mm, $x = 1.55$ mm) of the resonator. In all cases of the horizontally positioned FR, the width of the sample must be taken into account for comparison between computed and experimental values. As indicated in Table 6, the signal intensity on the upper surface of the FR amounts to 0.33. When the sample is located at the longest end of the FR, the signal intensity becomes 0.008, while the intensity of the signal at the lateral surface constitutes 0.04. Compared to the computed values presented in Table 6, there is good agreement between computed and experimental data.

Note that in both cases, when FR was in vertical or horizontal positions, on the upper surface (along axis z) EPR signal becomes three times smaller (0.33 compared to 1) than that in the center (at $z = 0$). Thus, accounting the effectiveness of this resonator ($G = 44$), it is possible to place the sample outside resonator, if necessary. For example, it becomes possible to apply a FR to investigate large samples or in vivo.

5. Conclusions

1. The calculated parameters, such as resonant frequency and dimensions of tested rectangular FRs, are in good agreement with correspondent experimental parameters. As for the computed magnetic field distribution, the comparisons within the experiment confirm the assumption that along the z axis, the magnetic field outside the resonator decays exponentially from its value at the boundary to zero at infinity. Another assumption that $H_z = 0$ at all surfaces parallel to the z axis (perfect open-circuit boundary conditions) is supported by the experiment only inside the FR. As the experiment demonstrates, the magnetic field exist and, evidently, decays exponentially outside lateral surfaces of the FR.
2. The dimensions (diameter and depth) of the sample hole play an important role in the efficiency of the FR. The greater the diameter of the hole (d) the smaller the magnetic field, (H) at the center of an FR. For FRs made of $KTaO_3$, the most significant improvement in signal intensity was achieved at $D = 0.9$ mm. At $D = 1.9$ mm the gain becomes more than twice as small.
3. Rectangular FRs are more effective than cylindrical ones. According to the results presented in [13], cylindrical FRs improved the sensitivity up to 10 times, while rectangular FRs achieved 44-fold improvement and even more for optimized geometry.
4. The optimized geometry of the FR is a hollow parallelepiped with $L/A(B)$ ratio around 2. It should be noted that an FR with the optimized dimensions, which was in the process of being tested at the time of this writing, improved the EPR signal by a factor of 100.
5. The results show the possibility of using an FR in EPR in vivo experiments, i.e., when sample is located outside the resonator.

Acknowledgments

The authors thank Tetyana V. Son'ko for growing the single crystals of potassium tantalate and express special thanks to Professor Gareth R. Eaton for the testing in his laboratory.

References

[1] R.G. Saifutdinov, L.I. Larina, T.I. Vakul'skaya, M.G. Voronkov, Electron Paramagnetic Resonance in Biochemistry and Medicine, Kluwer Academic, New York, 2001.
[2] G. Annino, M. Cassettari, I. Longo, M. Martinelli, Dielectric resonators in ESR: overview, comments and perspectives, Appl. Magn. Reson. 16 (1999) 45–62.
[3] A. Okaya, L.F. Barash, The dielectric microwave resonator, Proc. IRE 50 (1962) 2081–2092.
[4] R.W. Dykstra, G.D. Markham, A dielectric sample resonator design for enhanced sensitivity of EPR spectroscopy, J. Magn. Res. 69 (1986) 350–355.
[5] W.M. Walsh Jr., L.W. Rupp Jr., Enhanced ESR sensitivity using a dielectric resonator, Rev. Sci. Instrum. 57 (1986) 2278–2279.
[6] R. Biehl, The dielectric ring TE_{011} cavity, Bruker Report 1 (1986) 45–47.
[7] J. Wolak, B. Hilczer, Some applications of microwave ceramic ring resonator in laboratory measurements, Ferroelectrics 93 (1989) 73–76.
[8] A. Sienkiewicz, K. Qu, C.P. Scholes, Dielectric resonator-based stopped-flow electron paramagnetic resonance, Rev. Sci. Instrum. 65 (1994) 68–74.
[9] P. Hofer, R. Heilig, D.C. Maier, I. Prisecaru, D. Schmalbein, The superQ-FT accessory for pulsed EPR, ENDOR and ELDOR at 34 GHz, Bruker Spin Report 152/153 (2003) 37–43.
[10] I.N. Geifman, I.S. Golovina, V.I. Kofman, R.E. Zusmanov, The use of ferroelectric material for increasing the sensitivity of the EPR spectrometers, Ferroelectrics 234 (1999) 81–88.
[11] I.N. Geifman, I.S. Golovina, R.E. Zusmanov, V.I. Kofman, Raising the sensitivity of electron-paramagnetic-resonance spectrometer using a ferroelectric resonator, Tech. Phys. 45 (2000) 263–266.
[12] I.N. Geifman, I.S. Golovina, T.V. Son'ko, A ferroelectric resonator for EPR spectrometer, Patent of Ukraine 40178 (2001).
[13] Yu.E. Nesmelov, J.T. Surek, D.D. Thomas, Enhanced EPR sensitivity from a ferroelectric cavity insert, J. Magn. Reson. 153 (2001) 7–14.
[14] A. Blank, E. Stavitski, H. Levanon, F. Gubaydullin, Transparent miniature dielectric resonator for electron paramagnetic resonance experiments, Rev. Sci. Instrum. 74 (2003) 2853–2859.
[15] M.E. Il'chenko, E.V. Kudinov, Ferrite and Dielectric Microwave Resonators, Kiev University, Kiev, 1973.
[16] I.M. Buzin, I.V. Ivanov, N.N. Moiseev, V.F. Chuprakov, Nonlinearity and dielectric losses of potassium tantalate, Fiz. Tv. Tela 22 (1980) 2057–2062.
[17] S.H. Wemple, Some transport properties of oxygen-deficient single-crystal potassium tantalate ($KTaO_3$), Phys. Rev. 137A (1965) 1575–1582.
[18] Y. Fujii, T. Sakudo, Dielectric and optical properties of $KTaO_3$, J. Phys. Soc. Japan 41 (1976) 888–893.
[19] M.E. Lines, A.M. Glass, Principles and Application of Ferroelectrics and Related Materials, Clarendon Press, Oxford, 1977.
[20] I.M. Buzin, I.V. Ivanov, V.A. Chistyaev, V.F. Chuprakov, Low dielectric losses of nonlinear crystal—potassium tantalate, Pisma v Zh. Techn. Fiz. 6 (1980) 457–459.
[21] R.A. Laudise, The Growth of Single Crystals, Prentice-Hall, Englewood Cliffs, NJ, 1970.